Computer simulations of two-dimensional and three-dimensional ideal grain growth

Seong Gyoon Kim and Dong Ik Kim
Department of Materials Science and Engineering, Kunsan National University, Kunsan 573-701, Korea

Won Tae Kim
Division of Applied Science, Chongju University, Chongju 360-764, Korea

Yong Bum Park
Department of Materials Science and Metallurgical Engineering, Sunchon National University, Sunchon 540-742, Korea
(Received 21 February 2006; revised manuscript received 12 July 2006; published 27 December 2006)

We developed an efficient computation scheme for the phase-field simulation of grain growth, which allows unlimited number of the orientation variables and high computational efficiency independent of them. Large-scale phase-field simulations of the ideal grain growth in two-dimensions (2D) and three-dimensions (3D) were carried out with holding the coalescence-free condition, where a few tens of thousands grains evolved into a few thousand grains. By checking the validity of the von Neumann-Mullins law for individual grains, it could be shown that the present simulations were correctly carried out under the conditions of the ideal grain growth. The steady-state grain size distribution in 2D appeared as a symmetrical shape with a plateau slightly inclined to the small grain side, which was quite different from the Hillert 2D distribution. The existence of the plateau stems from the wide separation of the peaks in the size distributions of the grains with five, six, and seven sides. The steady-state grain size distribution in 3D simulation of the ideal grain growth appeared to be very close to the Hillert 3D distribution, independent of the initial average grain size and size distribution. The mean-field assumption, the Lifshitz-Slyozov stability condition, and all resulting predictions in the Hillert 3D theory were in excellent agreement with the present 3D simulation. Thus the Hillert theory can be regarded as an accurate description for the 3D ideal grain growth. The dependence of the growth rate in 3D simulations on the grain topology were discussed. The large-scale phase-field simulation confirms the 3D growth law obtained from the Surface Evolver simulations in smaller scales.

DOI: 10.1103/PhysRevE.74.061605 PACS number(s): 81.10.Aj, 61.50.Ah, 61.72.Mm

I. INTRODUCTION

The microstructural evolution of grain growth in terms of mean grain size and grain size distribution is important because they have strong influence on the mechanical, thermal, and electrical properties of engineering materials. Observation and analysis of the microstructures have been the first step in most basic researches on the development of advanced materials [1,2]. Grain growth takes place by boundary migration to reduce the total amount of grain boundary energy, while the force balance at each grain corner is maintained. The ideal grain growth is defined as a system where (1) both grain boundary energy σ and grain boundary mobility m are isotropic, (2) the force balance is maintained at each multiple junction of grain boundaries, (3) the migration rate v of a grain boundary is proportional to the mean curvature κ of grain boundary;

$$v = -m\sigma\kappa, \tag{1}$$

and (4) the coalescence of grains is not allowed or equivalently the orientations of all grains are different from each other. Even though the ideal grain growth is a simplified version of grain growth, exhaustive study on its dynamics is indispensable for understanding the real material.

Many computation tools have been proposed to simulate the grain growth phenomena; Monte Carlo Potts model [3–10], vertex model [11–17], Surface Evolver program [18–20], front tracking method [21,22], cellular automata model [23,24], finite element method [25], and phase-field model [26–31]. Despite very different ideas between models, they reach similar conclusions on the kinetic and topological aspects of two-dimensional (2D) and three-dimensional (3D) grain growth. The main conclusions they obtained are the parabolic growth kinetics in both 2D and 3D and the existence of time-independent grain size distribution (GSD) in the scaling regime. However, the GSDs obtained from 2D and 3D simulations during the last two decades appeared to be quite different from the prediction from the Hillert theory [32], even though they were slightly different from model to model. There seems to be a consensus that the original mean-field theory introduced by Hillert is not an accurate description of the ideal grain growth in both 2D and 3D. However, there still have been some limitations in the previous simulations, making the quantitative comparison with the theory inconclusive; large noise whose role in grain growth is unclear and lattice anisotropy in Monte Carlo simulation, grain coalescence due to limited number of grain orientations which is inhibited in the ideal grain growth, or limited number of grains in the computation system to get reliable statistics of grain growth.

There have recently been remarkable advances in the simulations of microstructural evolution by the phase-field models [33–39]. In the models, the boundary energy is introduced through gradient energy terms in free energy functional similar to the treatment of antiphase domain boundaries by Allen and Cahn [40]. The main advantage of this model is that continuous tracking of grain boundary position

is not required since the locations of grain boundaries are implicitly defined by the regions where the gradients of field variables are not zero. Also the Gibbs-Thomson effect is naturally incorporated in the governing equation. Another important feature of the phase-field model is that anisotropies in grain boundary energy and grain boundary mobility can be easily handled [28–30,34,36,39] and grid anisotropy is negligible as long as there are enough grid points to resolve the grain boundary region [36]. The disadvantage of the phase-field model in simulating grain growth is that the number of phase-field variables corresponding to grain orientations is limited due to a limit in computational resources [26–30], while the total number of different orientations in real materials is almost infinite. When the number of possible orientations is less than the total number of grains in the simulation system, there is a finite probability for grain growth to occur by coalescence, which is not allowed in the ideal grain growth. Coalescence will occur when two grains having a same orientation come into contact. At least 100 distinct grain orientations are needed to avoid a significant amount of coalescence during 2D phase-field simulations of grain growth [31]. As recently proposed by Krill and Chen [31], it is possible to avoid the coalescence of neighboring grains with a smaller number of orientation-field variables by dynamically reassigning the orientations of neighboring grains. But still approximately 20 order parameters are needed to eliminate the coalescence effect in 3D grain growth simulation [31]. Furthermore, this technique causes some difficulty in handling different grain boundary energies and mobilities, both of which are dependent on the relative orientation between neighboring two grains.

During 2D ideal grain growth, all individual grains should satisfy the von Neumann-Mullins equation [41,42]

$$\frac{dA_n}{dt} = \frac{\pi}{3} m\sigma(n-6), \tag{2}$$

where A_n is the area of a grain with n sides. According to this equation, grains having sides more than six will grow while grains with sides less than six will shrink and the changing rate of the grain area is only dependent on the number of edges, independent of time or grain size. To validate whether the simulation of the ideal grain growth is correctly being performed, therefore, one should test how well individual grains satisfy the von Neumann-Mullins equation. In the previous phase-field simulation, it was reported that many individual grains are violating the law [26,27]. For example, many small grains with seven sides had negative growth rates in that simulation. In the Monte Carlo simulations [4], fluctuation in growth rate was so strong that the system looked like to execute random walks in grain size space, rather than following the von Neumann-Mullins law. But in most other simulations of the ideal grain growth, there has been no test on the validity of the law for all individual grains. There thus seems to be some question whether the simulations of the ideal grain growth were correctly carried out. In this study we report large-scale phase-field simulations of 2D and 3D ideal grain growth, with greatly reduced memory requirement and improved computational efficiency. As an accuracy test of the simulations we show that most grains satisfy the von Neumann-Mullins law in 2D grain growth, indicating the simulation operates in a correct way. We then show for the first time that all assumptions and predictions in the Hillert 3D theory [32] can be reproduced from our simulations in a $420\times420\times420$ grid system.

This paper consists of five sections: Following this introductory section, we describe a phase-field model of grain growth which has been adopted for eutectic solidification by present authors [39]. A new algorithm for the efficient computation of the model is presented. Details of the simulation system and parameters are explained. In Sec. III, we test the von Neumann-Mullins law for all individual grains in a 2D system and then show the simulation results of the 2D ideal grain growth. In Sec. IV, the simulation results of the 3D ideal grain growth are presented. All assumptions and predictions in the Hillert 3D theory are tested and compared with the simulation results. Finally, in Sec. V, the difference between our simulation results and those obtained by other methods are compared and discussed.

II. MODELING AND SIMULATION METHOD

A. Phase-field model of grain growth

In the phase-field model, the grain boundaries are considered as diffuse interfaces, i.e., across a grain boundary region of a finite width, the orientation of a grain changes gradually into the orientation of the other grain. The orientation state of a point in a polycrystalline system consisting of Q grains is given by order parameter ϕ_q $(q=1,2,3,\ldots,Q)$. An integer q can be regarded as a number indicating a specific orientation of the grain, or simply a grain's name sorted by numbers. For clear definition of the phase-field ϕ_q, suppose a grain boundary between two grains named by $q=24$ and $q=57$ in the system. The state of the interior region of the grain with $q=24$ is defined as $\phi_{24}=1$ and $\phi_q=0$ for $q\neq24$. Across the grain boundary from the grain with $q=24$ to that with $q=57$, the phase field ϕ_{24} changes smoothly from one to zero and the phase field ϕ_{57} from zero to one, while $\phi_q=0$ for $q\neq24$ and $q\neq57$. We thus impose a condition that the sum of all phase-field values in a point (i,j,k) is conserved;

$$\sum_{q=1}^{Q} \phi_q(i,j,k) = 1. \tag{3}$$

The time-evolution equation of ϕ_q can be formulated by various ways [26,35,38,39]. In this study we follow the interface-field method which has been proposed by Steinbach and Pezzolla [38] and used for modeling eutectic solidification by the present authors [39]. This method has several merits in modeling grain growth as follows. First, the force balances at triple junctions are maintained for both the isotropic and anisotropic grain boundary energies [39]. Second, the anisotropies in interface energy and mobility as functions of misorientation and inclination can be easily implemented [39]. Third, the parabolic potential with a double obstacle is adopted, which results in a clear-cut boundary width without smearing phase field into grains [39]. In traditional methods with a ϕ^4 potential the phase field has a long tail smearing deep into the neighboring

grains. This property allows the interface field method to be effective in suppressing a spurious attractive interaction between two closely spaced interfaces. Here we outline the equations from the interface-field method, which are essential for simulating grain growth. Details of the model were described in [38,39].

We define a step function $s_q=1$ if $\phi_q>0$ and $s_q=0$ otherwise. Then the number of phases coexisting in a given point is

$$S(i,j,k)=\sum_{q=1}^{Q} s_q(i,j,k). \tag{4}$$

The evolution equation of the phase field is given by

$$\frac{\partial \phi_q}{\partial t}=\frac{2M_\phi}{S}\sum_{r\neq q}^{Q} s_r s_q\left(\frac{\partial F}{\partial \phi_q}-\frac{\partial F}{\partial \phi_r}\right), \tag{5}$$

where M_ϕ is the isotropic phase-field mobility and

$$\frac{\partial F}{\partial \phi_q}=\sum_{s\neq q}^{Q}\left(\frac{\epsilon^2}{2}\nabla^2\phi_s+\omega\phi_s\right), \tag{6}$$

where ϵ is the gradient energy coefficient and ω is the height of the parabolic potential with a double obstacle, assumed to be isotropic. The ideal grain growth in the present study is simulated by numerically solving Eq. (5).

The parameters ϵ, ω, and M_ϕ in Eqs. (5) and (6) have definite relationships with the energy σ, width 2ξ, and mobility m of grain boundary. Let us consider a grain boundary region between q and s grains, where the phase-field equation (5) is reduced to

$$\frac{\partial \phi_q}{\partial t}=M_\phi[\epsilon^2\nabla^2\phi_q-\omega(1-2\phi_q)], \tag{7}$$

and the same form holds for ϕ_s because $\phi_s=1-\phi_q$. Equation (7) is similar to the standard phase-field equation for two-phase system, except the last term in the right-hand side which is originating from the adoption of parabolic potential. The interface width 2ξ and grain boundary energy σ [39] for a boundary between two grains are given by

$$2\xi=\pi\frac{\epsilon}{\sqrt{2\omega}};\quad \sigma=\frac{\pi}{8}\epsilon\sqrt{2\omega}, \tag{8}$$

respectively. These relationships can be rewritten as $\omega=2\sigma/\xi$ and $\epsilon=(4/\pi)\sqrt{\xi\sigma}$.

The phase-field mobility M_ϕ has a relationship with the grain boundary mobility m. The relationship can be found by following Allen and Cahn [40]: Let us consider a shrinking q grain with a curvature κ;

$$-\frac{v}{M_\phi}\frac{d\phi_q}{dr}=\epsilon^2\frac{d^2\phi_q}{dr^2}+\epsilon^2\kappa\frac{d\phi_q}{dr}-\omega(1-2\phi_q) \tag{9}$$

in the spherical coordinate system, where we assumed an instantaneous steady state with the grain boundary velocity v and a thin-interface limit of $1/\kappa\gg\xi$. After multiplying $d\phi_q/dr$ on both sides, integrating Eq. (9) over the interfacial region $(1/\kappa-\xi<r<1/\kappa+\xi)$ yields

$$v=-M_\phi\epsilon^2\kappa, \tag{10}$$

where the first and last terms in the right-hand side of Eq. (9) disappeared after the integration because $\phi_q\to 0$ and $d\phi_q/dr\to 0$ at $r\to 1/\kappa+\xi$ and $\phi_q\to 1$ and $d\phi_q/dr\to 0$ at $r\to 1/\kappa-\xi$. The resulting equation (10) becomes identical with Eq. (1) if we put

$$M_\phi=\sigma\frac{m}{\epsilon^2}=\frac{\pi^2}{16}\frac{m}{\xi}, \tag{11}$$

where we used Eq. (8). Under the relationships (8) and (11) between parameters and the thin-interface limit condition of $1/\kappa\gg\xi$, the phase-field equation (7) is mapped on the sharp interface equation (1).

B. Algorithm for effective phase-field computation

In a system with Q grains in N^3 (in 3D) grid system, the variable $\phi_q(i,j,k)$ has QN^3 elements. Thus an extremely large memory space is required if we treat the $\phi_q(i,j,k)$ variable directly on a large system where statistically meaningful results can be obtained. This problem was overcome by developing a simple scheme in the present study. The basic idea in the scheme is that all the Q components of phase fields need not to be saved in a grid. Preliminary computations of grain growth showed that on almost all grids the number of phase fields having positive values was less than six in 3D (five in 2D). In other words, the possibility that more than six grains in 3D meet together at a point is extremely low. This means that we can put a restriction on the maximum number (N_p) of the positive phase-fields coexisting on a grid, with negligible effect on the grain growth dynamics and with significant reduction of the required memory space.

In order to embody this simple scheme into our simulation, for each grid point the field names and their field values of the positive phase fields must be separately listed in the order of the values and then recorded on the memory. For this work, we introduce the following variables; real variables $p_n(i,j,k)$ for the phase-field values in the order of $1\geq p_1\geq p_2\geq\cdots\geq p_{N_p}\geq 0$, and integer variables $q_n(i,j,k)$ for the corresponding phase-field names in $1\leq q_n\leq Q$. Thus the phase field states on a grid are described by the N_p pairs of variables (p_1,q_1), $(p_2,q_2),\cdots,(p_{N_p},q_{N_p})$. As an example, consider a grid point where only three phase fields with the name numbers 16, 74, and 91 coexist with their values 0.13, 0.52, and 0.35, respectively. It then follows $p_1=0.52$, $p_2=0.35$, $p_3=0.13$ and $q_1=74$, $q_2=91$, $q_3=16$. Note that the number of total elements in $[p_n(i,j,k),q_n(i,j,k)]$ is $2N_pN^3$, which is much smaller than QN^3 in case of direct treatment of the $\phi_q(i,j,k)$ variable.

When (p_n,q_n) at previous time step are given on all grids, at current time step our computation on a (i,j,k) grid progresses according to following steps: (1) Call all the phase-field names q_n and their values p_n on the (i,j,k) grid and its nearest neighbor grids $(i\pm1,j\pm1,k\pm1)$. (2) Solve numerically the phase-field equation (5) only for the called phase fields, which yields the phase-field names and their values at current time step on the (i,j,k) grid. New phase-

field names can come into the (i,j,k) grid from its neighbors. In this stage, therefore, the number of positive phase-fields on a grid can be larger than N_p. (3) List the phase-field names and values at current time step in the order of the phase-field values. (4) Record the phase-field names and their values from first to the N_pth on memory, and then discard all the remaining phase fields behind N_pth order. If the number n of the positive phase fields at current time step is less than N_p, record only n phase-field names and their values. In this stage the total sum of the recorded phase-field values on the (i,j,k) grid may deviate from one, because there might be some discarded phase fields. (5) Reassign the phase-field values to satisfy the condition $\Sigma p_n(i,j,k)=1$. This can be straightforwardly done by replacing the p_n with the p_n^* defined as

$$p_n^* = p_n \Big/ \sum_{m=1}^{N_p} p_m(i,j,k). \tag{12}$$

Such correction turned out to be essential in our computations, otherwise the grain boundaries became unstable.

C. Measuring geometric characteristics

The radius of a grain was determined from the grain volume, assuming spherical shape. The volume of the grain with a phase-field name was obtained by simply summing up all the phase-field values with the name. This is based on the fact that all the phase-field names of grains are different from each other in our computational scheme.

The most important topological characteristic of grains in this study is the number of the faces of each grain in 3D (sides in 2D). In the grain boundary region, two or more phase fields coexist on a (i,j,k) grid; (p_1,q_1), (p_2,q_2), (p_3,q_3), etc., where $p_1 \geq p_2 \geq p_3$, etc. If $p_1 > 0.5$ and $0 < p_2 < 0.5$, then the q_2 grain can be regarded as a periphery grain facing with the q_1 grain. Therefore the number of the faces for a given grain (for example, name 123) can be found as follows: (1) Search all grids with $q_1=123$ and check the p_1, p_2, and q_2 values on those grids. (2) Record the name q_2 only if $p_1 > 0.5$, $0 < p_2 < 0.5$ and the name q_2 is new. We then have a list of grain names faced with the grain 123, where the total number of the names in the list is the number of the faces for the grain 123. Other topological characteristics such as the number of the edges and corners can be easily measured by similar ways.

D. Simulation system and parameters

The computation parameters were as follows: the isotropic grain boundary energy $\sigma=1$, the grid size $\Delta x=\Delta y=\Delta z=1$, and the phase-field mobility $M_\phi=1$. We took the grain boundary width as $2\xi=6\Delta x$, which appeared to be a good compromise between high computational efficiency and negligible grid anisotropy. Then the parameters in Eq. (6) are determined as $\epsilon=4\sqrt{3}/\pi$ and $\omega=2/3$ from Eq. (8). The time step was determined by $\Delta t=0.9\Delta x^2/(\alpha M_\phi \epsilon^2)$, where $\alpha=6$ in 3D and $\alpha=4$ in 2D computations. 2D and 3D simulations were carried out on 2400×2400 grids and $420\times420\times420$ grids, respectively. The initial total numbers (Q) of grains were about 20 000–100 000 both in 2D and 3D simulations, depending on our choices of initial GSD and average grain size. The initial GSDs for computation were obtained by putting spherical (circular in 2D) grains on the randomly sampled positions in the system. The radii of the grains also were randomly sampled within a predetermined range, by which we could control the initial GSD and the average grain size. The names from 1 to Q in the sequence generating grains were given to all the initial grains in the system. In our computation scheme these initial names of grains are conserved unless they disappear from the system. In order to minimize the boundary effect on the grain growth kinetics, the periodic boundary conditions were imposed on all the boundaries of the system.

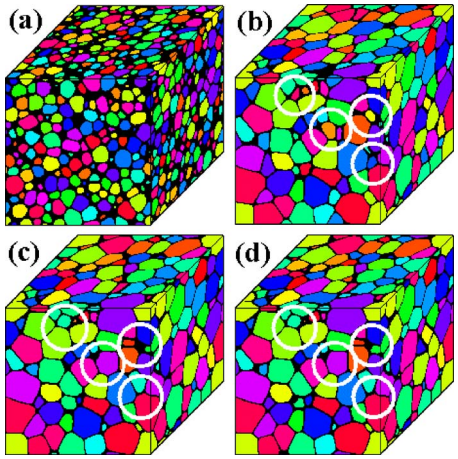

FIG. 1. (Color online) The effect of N_p (the number of the phase-fields allowed at a given grid point) on the microstructural evolution. (a) Computation with $N_p=10$ to $t=100\Delta t$ and further computations with (b) $N_p=4$, (c) $N_p=6$, and (d) $N_p=10$ to $t=1500\Delta t$. The computations were carried out in a $150\times150\times150$ grid system. As can be seen in the regions marked by the white circles, the microstructure computed with $N_p=6$ is almost identical to that with $N_p=10$, whereas there exists clearly discernable difference between microstructures with $N_p=4$ and $N_p=6$.

To reduce required memory space, the phase-field state (p_n,q_n) was recorded as an integer variable of ten digits, where the first five digits and the remaining five digits denote the phase-field name q_n and the phase-field value p_n, respectively. Most computations were proceeded until about 2000 (or 3000) grains remained in the 3D (2D) system, which took about 4000 (or 6000) time steps in 3D (2D) simulations. A typical computation with $420\times420\times420$ grids and 4000 time steps required six days on a personal computer with a 2.8 GHz CPU and 2 GB RAM.

N_p was determined from preliminary computations: In 3D simulations on a $150\times150\times150$ grid system, the effect of N_p on microstructural evolution is shown in Fig. 1. The simulation was started with $N_p=10$ and the microstructure at $t=100\Delta t$ is shown in (a). Then additional computations with sudden changes in N_p were performed. The resultant microstructures at $t=1500\Delta t$ are shown in (b) $N_p=4$, (c) $N_p=6$, and (d) $N_p=10$. As can be seen in the regions marked by white circles, the microstructure computed with $N_p=6$ is al-

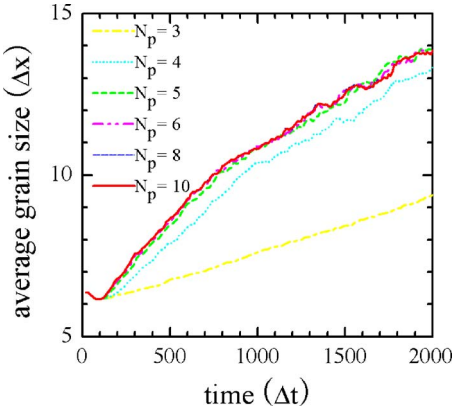

FIG. 2. (Color online) The effect of N_p on the changes of the average grain size with time in a $150\times150\times150$ grid system. The data were taken from the simulations of Fig. 1. With increasing N_p, the evolution curves with time converge to the case with $N_p=10$. Three curves with $N_p\geq6$ were almost perfectly overlapped.

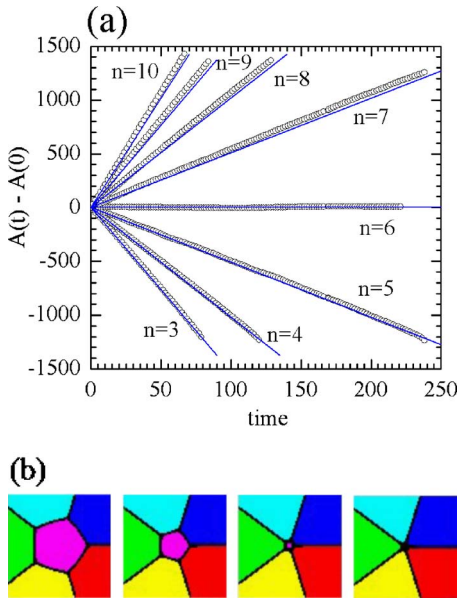

FIG. 3. (Color online) Time-evolutions of the n-sided regular polygonal grains. (a) Changes of grain area with time. The circles indicate the simulation results and the straight lines depict the predictions by the von Neumann-Mullins law. (b) An example of the time-evolution of a regular pentagonal grain, where four successive microstructures were taken at $t=17$, 170, 239, and 241, respectively.

most identical to that with $N_p=10$, whereas there exists some clearly discernable difference between the microstructures computed with $N_p=4$ and $N_p=6$. Figure 2 show the effect of N_p on the average grain size evolution with time. The data were taken from the simulations shown in Fig. 1. We can see that with increasing N_p the evolution curve converges to the case with $N_p=10$ and three curves with $N_p\geq6$ are almost perfectly overlapped. Thus the best compromise between small memory space and negligible effect on the grain growth kinetics appears to be $N_p=6$ in 3D computations. We also carried out similar preliminary simulations for 2D grain growth and found that $N_p=5$ is a good choice. Throughout the present study, therefore, we took $N_p=5$ and $N_p=6$ in 2D and 3D computations, respectively.

III. 2D SIMULATION RESULTS

The ideal grain growth in 2D has been extensively studied by simulations [3–8,11–15,18,19,21–27] and theoretical approaches [32,43–54]. All individual grains during ideal grain growth in 2D should satisfy the von Neumann-Mullins equation (2). Thus this section is concentrated on the following. The first is to test whether our simulations are correctly operating under the condition of ideal grain growth, that is, how well the individual grains in our simulations satisfy the von Neumann-Mullins law. The second is to find the GSD at steady state.

A. von Neumann-Mullins law

By using the relationships (11), the von Neumann-Mullins equation (2) can be written as

$$\frac{dA_n}{dt}=\frac{16}{3\pi}\xi M_\phi\sigma(n-6)=\frac{16}{\pi}(n-6), \tag{13}$$

where we took $\xi=3\Delta x=3$, $M_\phi=1$, and $\sigma=1$ used in the simulations as explained in Sec. II. The test of Eq. (13) was carried out by two different ways; continuous tracking of the changing rate of the grain area for a regular polygonal grain surrounded by n grains and checking the rates for all individual grains in the system undergoing grain growth.

First, we show the time-evolutions of the n-sided regular polygonal grains. For the grains with $n\leq6$, their area changes from an initial area of about $1200\Delta x^2$ were tracked until they shrank to disappear except for the case with $n=6$. For the grains with $n>6$, their growing area changes from an initial area of about $25\Delta x^2$ were tracked. The results are shown in Fig. 3(a), where the circles indicate the simulation results and the straight lines indicate the predictions by Eq. (13). (During the simulation, the boundaries between periphery grains remained straight by keeping the phase-field values at the system boundaries unchanged.) The current simulations are in excellent agreement with the predictions by Eq. (13). Even though the discrepancies between them tend to increase with growth of grains having more than six sides, it appeared to be within a few percent. An example of the time-evolution of a regular pentagonal grain is given in Fig. 3(b), where four figures depict the microstructures at $t=17$, 170, 239, and 241. The pentagonal grain is shrinking with time because its sides are slightly convex. Equilaterality of the pentagonal grain is being well maintained until the moment of its disappearance. This implies that the lattice anisotropy effect in the simulation is negligible.

Figure 4(a) shows the change rates of grain area dA/dt of 4331 individual grains plotted with the normalized grain radius $r/\langle r\rangle$ at $t=205$ in 2D grain growth on 2400×2400 grid system. The average grain radius $\langle r\rangle$ was $19.2\Delta x$. The values of dA/dt were measured from the changes during a single time step. The side numbers of individual grains were discriminated by different symbols. The arrow marks with each side number denote the theoretical predictions by Eq. (13).

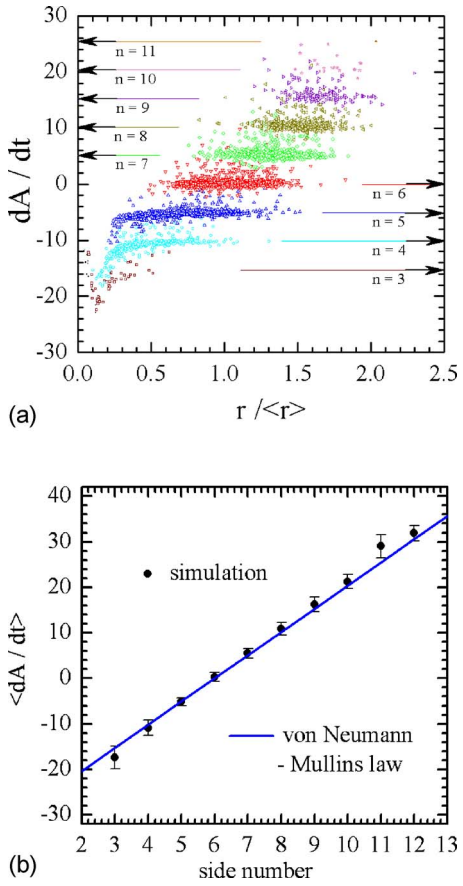

FIG. 4. (Color online) (a) Area change rates dA/dt of 4331 individual grains plotted with the relative grain size at $t=205$ in the 2D grain growth. The side numbers of individual grains were discriminated by different symbols. The arrow marks denote the predictions by the von Neumann-Mullins law. (b) Average area change rates $\langle dA/dt \rangle$ and their standard deviations plotted with the side numbers of grains. The straight line depicts the prediction by the von Neumann-Mullins law.

As can be seen from this figure, the values of dA/dt are independent of the grain size and the dots with a same number of sides are mostly located along a horizontal line predicted by Eq. (13). It appeared that all 850 seven-sided grains grew and 1212 of 1215 five-sided grains (blue dots) shrank regardless of their grain size. At the early stage of simulation, however, the fluctuation in dA/dt was relatively large. For example, at $t=17$ with $\langle r \rangle = 8.7\Delta x$, it appeared that 98.7% grains of the seven-sided grains grew and 96.1% grains of the five-sided grains shrank. In the region with $r \leq 0.25\langle r \rangle = 4.8\Delta x$, the grains shrink faster than the predicted rates. The grain radius r in that region is smaller than the interface width $2\xi = 6\Delta x$. Therefore one of the sources causing this anomalous behavior may arise from the violation of the thin interface limit condition $r \gg 2\xi$. Another probable source is the error inevitable in enumerating the sides for such small grains comparable with the interface width. However, this anomalous behavior seems to have negligible effect on the overall dynamics of grain growth because the fraction of such small grains was small, that is, 80 grains of total 4331 grains. Figure 4(b) shows the average area change rates

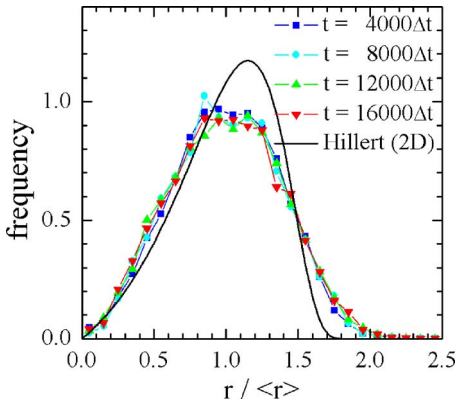

FIG. 5. (Color online) Grain size distributions in the 2D grain growth in a 2400×2400 grid system. The numbers of grains decreased from 12 618 at $t=1500\Delta t$ to 3555 at $t=6000\Delta t$.

$\langle dA/dt \rangle$ plotted with the side number of grains, where the error bars denote the standard deviations and the straight line is the prediction by the von Neumann-Mullins equation (13). For grains with $4 \leq n \leq 10$ where 4268 of the total 4331 grains are included, the simulation results are in good agreement with the prediction within a few per cent error. Relatively large deviation from prediction for the 46 grains with $n=3$ is due to high fraction of small grains comparable to the interface width, as in the region with $r \leq 0.25\langle r \rangle$ in Fig. 4(a). The large deviation for the 17 grains with $n \geq 11$ seems to originate from poor statistics due to their small number of the grains. From Figs. 3 and 4 we can conclude that the present phase-field computations are simulating the ideal grain growth in quantitatively correct way.

B. 2D grain size distribution

A typical GSD is shown in Fig. 5, which was obtained from a 2D simulation on a 2400×2400 grid system, where symbols are the simulation results at the indicated time steps and the thick curve is the prediction by the Hillert 2D theory. The initial number of grains was about 60 000. The GSD in the system reached the steady state after 1000 Δt when 18 054 grains survived. Even though the computation was continued to $t=6000\Delta t$ when about 3555 grains survived, the GSD remained almost unchanged as can be seen in the figure, which indicates that a steady-state GSD was reached. However, the GSD was far from that of the Hillert 2D prediction.

To check the effect of the initial GSD on the steady-state GSD, we simulated 2D ideal grain growth with three different initial GSD and different average grain sizes in a range of $(8-12)\Delta x$, as shown in Fig. 6(a). The resultant GSDs averaged over time duration $t=(1500-6000)\Delta t$ were almost identical to each other, as shown in Fig. 6(b). Thus we believe that the profile in the figure corresponds to a universal shape of the 2D steady-state GSD, which is quite different from that predicted by the Hillert 2D theory. This GSD has two distinguished characteristics: First, while the GSD from the theoretical prediction is asymmetric, the simulated GSDs are almost symmetrical with respect to $r/\langle r \rangle = 1$. Second, the

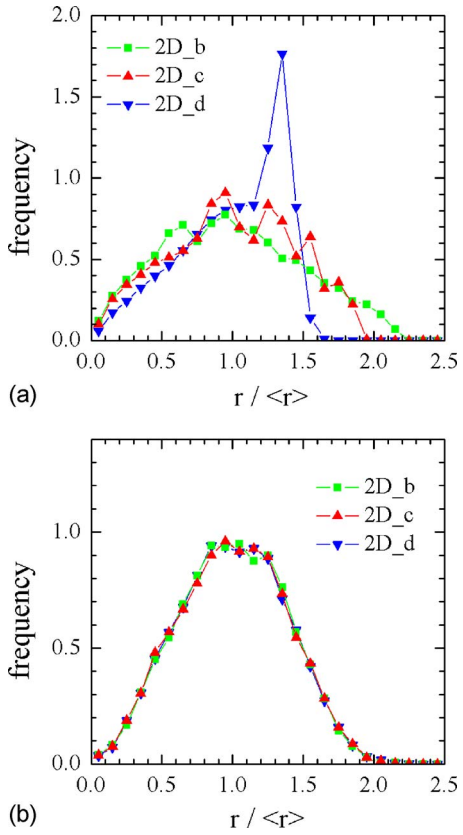

FIG. 6. (Color online) Effect of the initial condition on the steady-state grain size distribution in the 2D grain growth in a 2400×2400 grid system; (a) three different distributions at the early stage ($t=40\Delta t$) and (b) the distributions averaged over duration $t=(1500-6000)\Delta t$ after reaching the steady state.

simulated GSDs exhibit plateaus slightly inclined to the small grain side. The former is well known now; most of the 2D simulations where the coalescence between grains is not allowed or sufficiently suppressed have shown similar symmetry [5,7,11,12,14,15,55]. The latter has not been observed in most previous simulations, but reported in a few simulations using the vertex model [11,14,15]. Even though the existence of the plateau has not received much attention up to now, it seems to be an important characteristic of 2D ideal grain growth to be explained.

We also checked the exponential time-dependence of the average grain size from simulations. The exponent was very close to two as expected, as long as the data are taken within the steady-state regime.

IV. 3D SIMULATION RESULTS

With recent advances in computing power and simulation method, various 3D simulations of the ideal grain growth have been carried out [8–10,16,17,20,23,24,31]. They have shown that as in the 2D case the GSD in the 3D ideal grain growth is also different from the Hillert 3D distribution [32], which has recently been well summarized by Krill and Chen [31]. In this section we present the simulation results of the 3D ideal grain growth in a large system where a few tens of

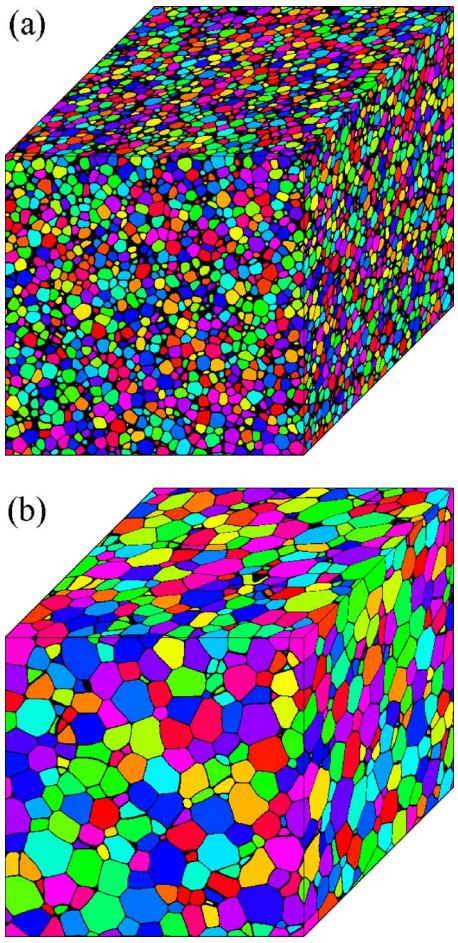

FIG. 7. (Color online) A typical microstructure evolution during the 3D ideal grain growth in a $420\times420\times420$ grid system; (a) 28 181 grains at $t=100\Delta t$ and (b) 2012 grains at $t=4000\Delta t$.

thousands grains evolve into a few thousand grains. It will be shown that our GSD is just that of Hillert, and then all assumptions and predictions of the Hillert 3D theory will be compared with simulations.

Figure 7 shows a typical simulated evolution of microstructure during a 3D ideal grain growth on a $420\times420\times420$ grid system. Among the 28 181 grains at $t=100\Delta t$ in (a), 2012 grains survived at $t=4000\Delta t$ in (b). Note that the system volume is about 13 times larger than that in the recent phase-field computations by Krill and Chen [31].

A. 3D grain size distribution

The evolution of GSD in early stage of 3D grain growth on $420\times420\times420$ grid system is shown in Fig. 8(a). The GSD profile changed rapidly at the initial stage toward a steady state, and after $t=400\Delta t$ it reached a steady-state distribution which is almost perfectly matched with the Hillert 3D distribution. As shown in Fig. 8(b), the distribution remains unchanged after $t=400\Delta t$ although the number of grains decreased from 18 445 at $t=400\Delta t$ to 2630 at $t=3200\Delta t$. Note that all the profiles correspond to the instantaneous distributions at the indicated times. We continued the computation to $t=8000\Delta t$ when 785 grains survived in the

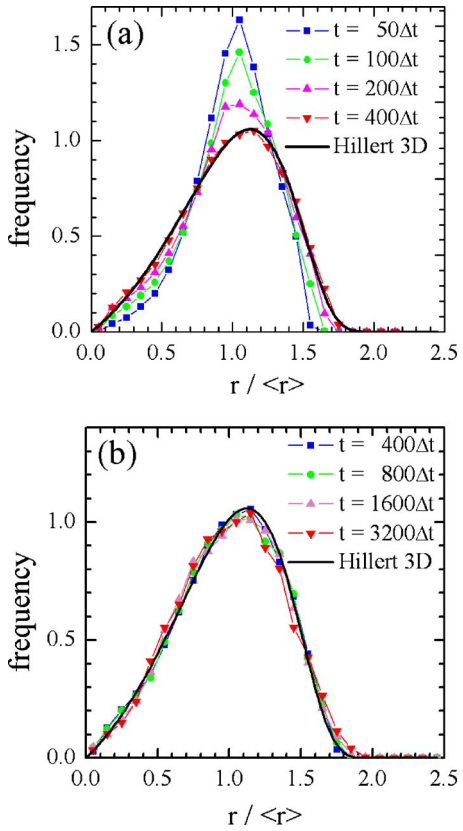

FIG. 8. (Color online) Evolution of the grain size distribution during the 3D ideal grain growth in a $420\times420\times420$ grid system. (a) Distribution profiles at different time steps of $50\Delta t$, $100\Delta t$, $200\Delta t$, and $400\Delta t$ move toward the steady state and (b) after $t=400\Delta t$ the grain size distribution remains unchanged at the steady state which corresponds to the Hillert distribution. The initial number of grains was 29 320, which decreased to 18 445 at $t=400\Delta t$ and 2630 at $t=3200\Delta t$. All curves show the instantaneous distributions at the times indicated.

system. The distributions averaged over the interval of about $100\Delta t$ still remained unchanged although the instantaneous distributions showed large statistical fluctuation.

The effect of the initial GSD on the steady-state GSD is shown in Fig. 9. Three different GSDs at an early stage ($t=100\Delta t$) are shown in Fig. 9(a), where the numbers of grains were 38 349, 28 181, and 21 911 for the distributions denoted by squares, triangles, and inverted triangles, respectively. Despite the different initial GSDs and different average grain sizes, all the distributions were converged to the Hillert distribution as grain growth undergoes. The time-averaged distributions after reaching the steady state are shown in Figs. 9(b), 9(c), and 9(c), which evolved from the three different initial distributions shown in Fig. 9(a). The initial conditions affected only the transient time for reaching the steady state. Thus the steady-state GSD obtained from our large-scale simulations shows striking congruence with the Hillert 3D distribution in all respects; the asymmetry in the profile, a peak at $r=(9/8)\langle r\rangle$ and cutoff at around $r=2\langle r\rangle$. We could not find any grain twice larger than the average grain size in the three simulations of Fig. 9, as far as the system reached the steady state.

B. Comparison with Hillert 3D theory

The Hillert theory [32] uses two keys to solve the ideal grain growth problem. The first is the mean-field approximation for each grain's growth rate

$$\frac{dr}{dt}=M\left(\frac{1}{r_c}-\frac{1}{r}\right);\quad r\frac{dr}{dt}=M\left(\frac{r}{r_c}-1\right), \tag{14}$$

where r_c is a critical grain radius to be determined later and M is a constant. The next key which leads the system to the existence of a steady state is the Lifshitz-Slyozov (LS) stability condition

$$\frac{d\rho}{d\tau}=-\frac{(\rho-2)^2}{2\rho}, \tag{15}$$

where $r=\ln r_c^2$ and $\rho=r/r_c$. Hillert obtained this condition by following the way that Lifshitz and Slyozov [56] solved the particle coarsening problem. All predictions in the Hillert theory are rigorously derived from Eqs. (14) and (15), which can be listed as follows [31] for 3D case. First, the square of the average grain size $\langle r(t)\rangle^2$ is a linear function of time:

$$\langle r(t)\rangle^2-\langle r(0)\rangle^2=kt, \tag{16}$$

where $\langle r(0)\rangle$ is the initial average grain size and k is a constant. Second, two constants M in Eq. (14) and k in Eq. (16) are not independent, but correlated by

$$\frac{k}{M}=\frac{1}{2}\left(\frac{8}{9}\right)^2=0.395. \tag{17}$$

Third, the critical radius r_c in Eq. (14) is given by

$$r_c=(9/8)\langle r\rangle. \tag{18}$$

Therefore the grains with $r>(9/8)\langle r\rangle$ grow, while the other grains shrink. And last, the GSD at the steady state is given by

$$F(\rho)=(2e)^3\frac{3\rho}{(2-\rho)^5}\exp\left(-\frac{6}{2-\rho}\right). \tag{19}$$

From now on, we test all assumptions and predictions of the Hillert 3D theory.

The validity of the mean-field equation (14) can be checked by plotting rdr/dt values of grains against $r/\langle r\rangle$. The result obtained from the simulation at $t=3000\Delta t$ is shown in Fig. 10, where 1400 grains randomly sampled from the total 2837 grains were shown as dots in a rdr/dt vs $r/\langle r\rangle$ plane. The dr/dt values were measured from the radius changes during a single time step. The grains with 9–20 faces, which occupy 77% of the total grains, were discriminated by different symbols and the indicated numbers denote the number of faces. As can be seen from this figure, the dots corresponding to neighboring topological classes are not only significantly overlapped, but also concentrated along a line. The horizontal spread width of the dots from each class is as small as about $0.5\langle r\rangle$. These features are in contrast with the 2D case shown in Fig. 4(a), where the horizontal spread widths of the dots approaches about $\langle r\rangle$ and the discreteness between topological classes is very strong. The distribution

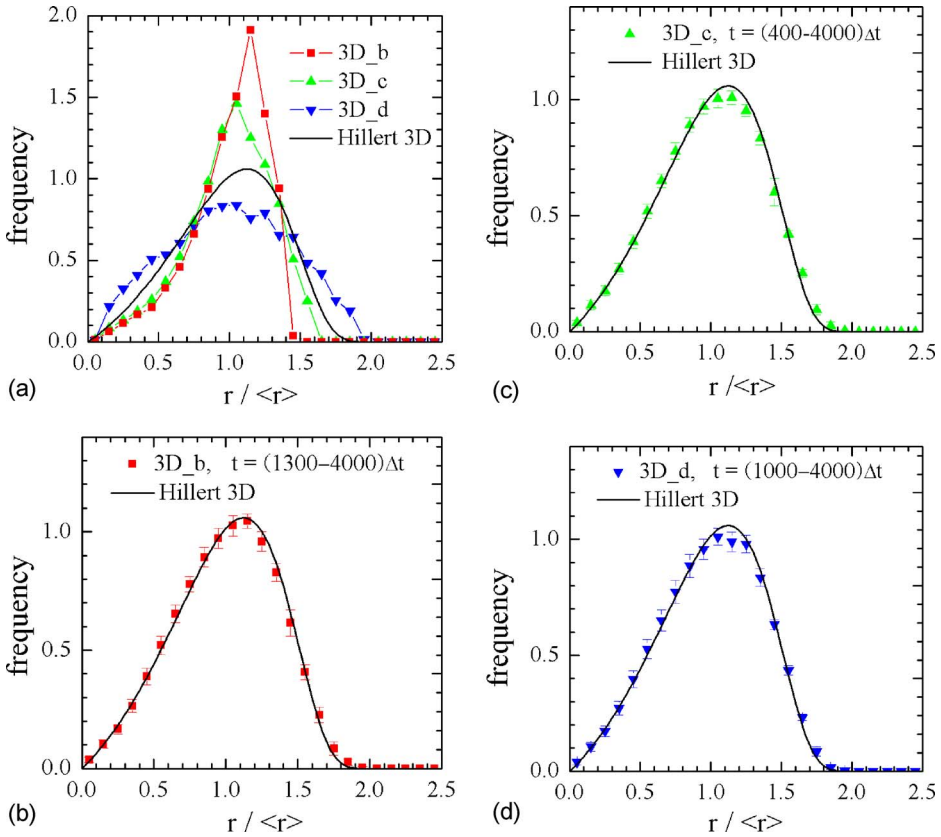

FIG. 9. (Color online) Effect of initial conditions on grain size distribution in a 3D grain growth in a $420\times420\times420$ grid system. (a) Three different distributions at an early stage ($t=100\Delta t$), where the numbers of grains were 38 349, 28 181, and 21 911 for the distributions denoted by squares, triangles, and inverted triangles, respectively. (b)–(d) Time-averaged distributions after the system reached the steady state, which evolved from three distributions shown in (a).

of the dots in Fig. 10 can be well represented by a thick straight line which is the linear least-square fitting over all the points appearing in Fig. 10. Therefore we conclude that the mean-field equation (14) can be considered as a good approximation for the growth rate of each grain conducting the 3D ideal grain growth, but not for the 2D growth. Also it

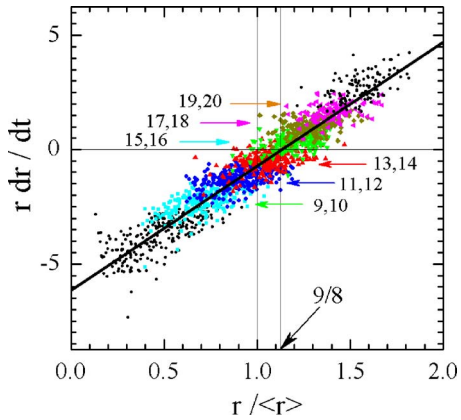

FIG. 10. (Color online) Simulation test of mean-field approximation [Eq. (14)] in the 3D ideal grain growth. 1400 grains randomly sampled from about 2837 grains at $t=3000\Delta t$ were shown as dots in a rdr/dt vs $r/\langle r\rangle$ plane. The dr/dt values were measured from the changes during a single time step. The grains with 9–20 faces were discriminated by symbols, where the numbers written count the faces of the grain. The thick straight line is the linear least-square fitting over all the points in the figure. Note that $r=r_c=\langle r\rangle$ 9/8 when dr/dt on this line, as predicted in the Hillert 3D theory.

should be noted that the dr/dt value on the fitted straight line becomes almost zero at $r=(9/8)\langle r\rangle$, which remained unchanged as long as the system is in the steady-state regime. This is a confirmation of the prediction (18) from the Hillert 3D theory.

In order to test if the LS stability condition (15) is justified in simulation, we measured the $d\rho/d\tau$ values for all grains in the system by using an approximation

$$\frac{d\rho}{d\tau}=\frac{d(r/r_c)}{d\ln r_c^2}\simeq\frac{4}{9}\frac{r^{t+\Delta t}/\langle r\rangle^{t+\Delta t}-r^t/\langle r\rangle^t}{\ln\langle r\rangle^{t+\Delta t}-\ln\langle r\rangle^t}. \tag{20}$$

The radii r^t and $r^{t+\Delta t}$ of each grain at previous and current time steps can be directly read out in simulation. But there is a problem in measuring the average radii $\langle r\rangle^t$ and $\langle r\rangle^{t+\Delta t}$; even though the average grain size $\langle r\rangle$ is a smoothly increasing function of time on a long time scale, it can fluctuate significantly on a scale of a few time steps. This is because $\langle r\rangle$ varies very sensitively with the number of grains disappearing from the system. For example, let us consider a short time duration without any disappearing grains in the system. During that time, the shrinking rates of the small grains must be faster than the growing rates of the large grains as far as the total mass of the system is conserved, and the average grain size decreases with time. Therefore taking the instantaneous values for $\langle r\rangle^t$ and $\langle r\rangle^{t+\Delta t}$ must be avoided. Instead we took them from the time-evolution of $\langle r\rangle$ fitted with Eq. (16) over the steady-state regime. Figure 11 shows the $d\rho/d\tau$ values (small circles) for all grains in a system at $t=3000\Delta t$, which were measured by using Eq. (20). The circles were strongly clustered along a curve which is just the

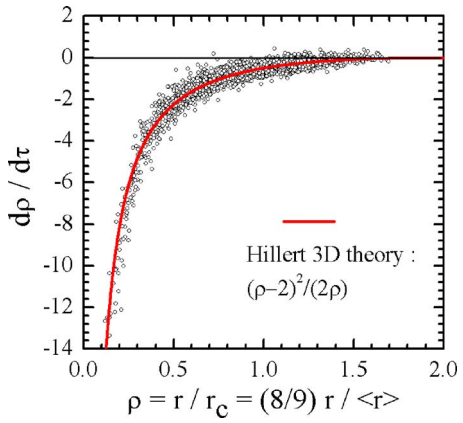

FIG. 11. (Color online) Test of LS stability condition in the 3D grain growth. All the grains at $t=3000\Delta t$ were shown as circles in a $d\rho/d\tau$ vs ρ plane and the curve depicts the stability function $-(\rho-2)^2/(2\rho)$ in the Hillert theory.

stability function $-(\rho-2)^2/(2\rho)$ in the Hillert theory. Such agreement was maintained as long as the system is in the steady-state regime.

Our simulations showed that the mean-field assumption and the LS stability condition in the Hillert theory are well satisfied in 3D ideal grain growth. All the predictions in the theory follow from the mean-field assumption and the LS stability condition. Including the steady-state GSD shown already, therefore, all the other predictions from the theory should be in good agreement with those from the simulations. For further confirmation, we proceed to test the remaining predictions (16) and (17).

Figure 12(a) shows the time evolution of the average grain size in 3D grain growth. The circles are the simulation result and the solid curve is a nonlinear least-squares fitting with Eq. (16) over the time interval $400\Delta t \le t \le 4000\Delta t$ ($\Delta t = 0.0308$) of the steady-state regime. Because in the fitting a small change in the exponent n results in big change in the k value, we fixed the n value as $n=2$. As expected, the fitted curve was in good coincidence with the simulated data, and the resultant k value was 2.38.

The mean-field constant M in Eq. (14) was obtained from the slope of the linear least-square fitting shown in Fig. 10. The variation of M with time is shown in Fig. 12(b). After the system reached the steady state at about $t=400\Delta t$, M varied slightly in a range of 5.9 ± 0.4 with time. From these k and M values, we find $k/M \simeq 0.40$ in simulations, which is very close to the predicted value 0.395 in Eq. (17).

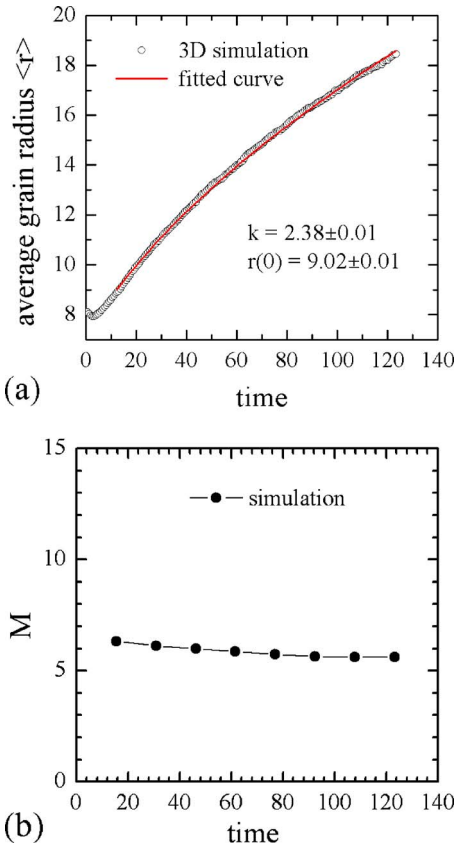

FIG. 12. (Color online) (a) Time evolution of the average grain size in the 3D grain growth. The circles and solid curve, respectively, indicate the simulation result and a nonlinear least-squares fitting with Eq. (16) over the time interval $400\Delta t < t < 4000\Delta t$ ($\Delta t = 0.0308$) with a fixed exponent $n=2$. The k value from the fitting is 2.38. (b) The variation of the mean-field constant M in Eq. (16) with time. After reaching the steady state at about $t=400\Delta t$, M varies slightly in a range of 5.9 ± 0.4 with time.

V. DISCUSSION

As shown in previous sections, all details of the Hillert 3D theory as well as its GSD were in excellent agreement with our 3D simulations. On the other hand, the distribution obtained from the 2D simulations is significantly deviated from that of the Hillert 2D theory. We will discuss first what causes the difference between 2D and 3D simulations. The Hillert theory based on the mean-field approximation which assumes that the growth rate of a grain is governed by interaction between its own field (own size) and a mean field (the average grain size of matrix). However, the growth rate of an individual grain is governed by the interaction between its own field and local field (the average grains size of its nearest neighbors), not the mean field. Therefore the applicability of the mean-field theory depends on how closely the mean field represents the local field; it must be much better for 3D system with 13.4 nearest neighbors (our computation) on average than for 2D system with 6 neighbors, because with increasing nearest neighbors the local field will statistically become closer to the mean field.

The GSDs in our simulations appeared to be somehow different from those of the previous simulations, especially in 3D. In the remaining part of this section, we compare our simulations with the previous simulations, and then discuss the differences in terms of possible origins.

A. Comparison with previous 2D simulations

There have been several 2D simulations carried out by various methods including Monte Carlo Potts model [3–8], phase-field model [26–30], vertex model [11–15], front tracking method [21,22], and cellular automata method [23,24]. Most of them showed that the scaling law $\langle r \rangle^2 \sim t$ is

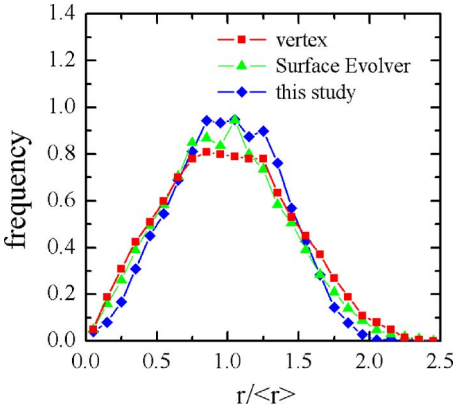

FIG. 13. (Color online) The distributions obtained from the deterministic models. The squares are from the vertex model [15], triangles from the Surface Evolver program [18], and diamonds from the present phase-field model, respectively. The distribution from the Surface Evolver program is similar with that from this study, except for a clear evidence of the plateau. The simulations based on five different vertex models always showed the existence of the plateau, of which only one was shown in this figure.

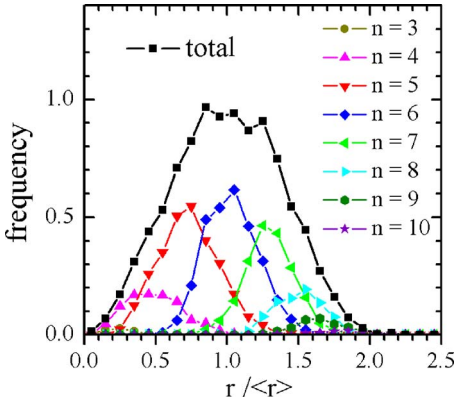

FIG. 14. (Color online) Size distribution of each topological class. The squares are the overall size distribution contributed by all grains and the other symbols are the size distributions for the topological classes denoted by indicated numbers. Note the peak heights and peak positions of the size distributions with $n=5$, 6, and 7. Such distribution profiles of the major topological classes are combined to form a plateau with small undulations in overall size distribution for all grains.

valid and there exists a steady-state GSD. The GSD shapes appeared to be quite different from the Hillert distribution. Those from the Monte Carlo simulations [3–8] appear to be similar with each other; symmetrical shape with a peak maxima at $r=\langle r\rangle$ without the plateau shown in Fig. 6(b). The GSDs obtained by Surface Evolver program [17], vertex model [15], and present phase-field model, which belong to the deterministic model are shown in Fig. 13. The GSD from Surface Evolver program is similar to that from this study, but except for clear evidence of the plateau. On the other hand, the simulations based on five different vertex models [15], of which only one was shown in the figure, always showed the existence of the plateau, even though its height was lower than that from this study.

The formation of the plateau on the GSD in the present simulation can be readily understood by plotting the GSDs of each topological class, which is shown in Fig. 14. In this figure the squares are the overall GSD contributed by all grains and the other symbols are the GSDs of the topological classes denoted by the indicated numbers. It is noted that the grain size increases with increasing n and those grains with $n=5$, 6, and 7 are the major contributors to the overall GSD. The size distributions of the grains with $n=5$, 6, and 7 are rather similar in shape and have similar heights spaced by about 0.3 $\langle r\rangle$. When such distribution profiles of the topological classes are combined into an overall GSD, it is inevitable to form a plateau with small undulations. To fully understand the 2D ideal grain growth, including the existence of a plateau in the GSD, analysis of GSDs for each class will be needed. Theoretical work in this direction may be based on the time evolution of two-parameter distribution function $f(n,r,;t)$, as in Abbruzzese *et al.* [43,44] and Pande and Rajagopal [51].

It is worthwhile to compare the present 2D phase-field simulation with Fan and Chen's phase-field simulation [26,27]. The main difference between the two models is in the form of double-well potential in governing equation; a ϕ^2-type with double obstacles in the former and a ϕ^4-type in the latter. In principle, the phase-field simulations of grain growth should yield a similar result irrespective of the detailed forms of the adopted double-well potential. But there seems to be apparent differences between the results from the present simulation and Fan and Chen's simulation; GSD and the fluctuation in the area change rates of grains. However, the GSDs cannot be directly compared with each other because the coalescence between grains was not ignorable in the Fan and Chen simulation where only 36 grain orientations were allowed. The difference in the area change rates of grains looks significant, as can be seen from comparison between Fig. 4 of this paper and Fig. 9 in [27]. In fact, the area change rates in [27] were taken at an early stage ($\langle r\rangle \simeq 8\Delta x$) of the simulation, where the grain radius is close to the boundary width. In this stage, there may be not only large error in counting the number of sides for a grain, but also somewhat violation of the thin interface limit condition $r \gg 2\xi$ under which the phase-field equation (7) is reduced to Eq. (1) of sharp interface motion. If the data were taken at a later stage, the fluctuation would be significantly reduced.

B. Comparison with previous 3D simulations

With recent advances in computing power and simulation method, various simulations of 3D ideal grain growth have extensively been carried out. These 3D simulations can be categorized into two groups; statistical models and deterministic models. The former is based on Monte Carlo Potts model [9,10], and the latter includes various models such as vertex model [16,17], Surface Evolver program [20], and phase-field model [31]. Krill and Chen have critically reviewed and compared them with the results from the phase-field simulation [31].

We compare the 3D GSD from our simulation with those from the previous simulations. Figure 15 shows the distributions from phase-field simulation by Krill and Chen [31]

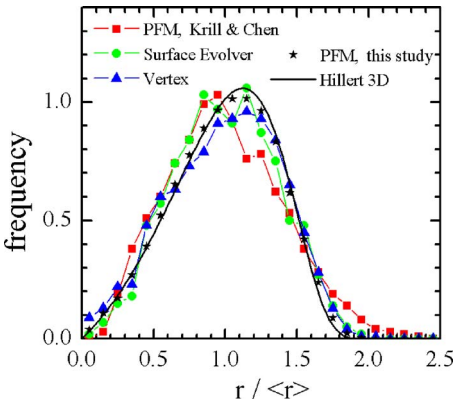

FIG. 15. (Color online) The steady-state grain size distributions from various simulations of the 3D ideal grain growth; the phase-field simulation by Krill and Chen [31] (squares), Surface Evolver program by Wakai *et al.* [20] (circles), vertex simulation by Weygand and Brechet [17] (triangles), and the present phase-field simulation (stars). The thick curve depicts the 3D distribution predicted by the Hillert theory.

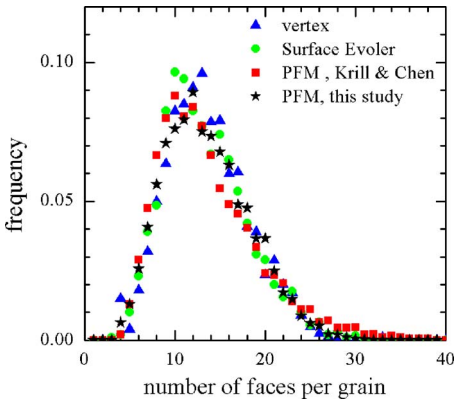

FIG. 16. (Color online) Distributions of grains with the number of faces per grain in the 3D simulations. Triangles denote the results from the vertex simulation [17], circles from the Surface Evolver program [20], squares from Krill and Chen [31], and stars from the present simulation, respectively.

(squares), Surface Evolver program by Wakai *et al.* [20] (circles), vertex simulation by Weygand and Brechet [17] (triangles), and our phase-field simulation (stars) which is an average of those in Figs. 9(b)–9(d), where the curve drawn by the thick line is the 3D distribution from the Hillert theory. Only the distributions from the deterministic models were shown in this figure, because the distributions from the Monte Carlo simulations were quite similar with that from the Krill and Chen phase-field simulation, as noticed by them [31]. Of four distributions in this figure, the Krill and Chen distribution looks somewhat unique because only the profile is rather symmetric against $r=\langle r\rangle$. In other words, the frequency between $\langle r\rangle$ and $1.5\langle r\rangle$ is lower than in the other three distributions, whereas the frequency over $1.5\langle r\rangle$ is significantly higher. In the other three distributions, the slopes at the right side are steeper than those at the left side, which is one of the characteristics in the Hillert 3D distribution. The distribution from the vertex model is quite similar to our distribution, even though the peak height is lower. It is of interest that similar behavior was also observed in the 2D simulations shown in Fig. 13. Even though the distribution from the Surface Evolver simulation shows large fluctuation around the maximum peak position, the right side of the profile seems to be close to the Hillert 3D distribution. However, it should be noted that the number of initial grains was no more than 1000 in the Surface Evolver simulation [20] and 5000 in the vertex simulation [17].

Considering that both the phase-field simulations in Fig. 15 are free from the grain coalescence, it is surprising that they yield quite dissimilar GSDs. One possible cause of the dissimilar distributions is the difference in the simulation conditions: The present 3D simulation system is 13 times larger than the previous one [31], and thus statistically more sensible results can be anticipated. Also it is noted that in the Krill and Chen simulation the distribution is systematically changing throughout the entire simulation time, as can be seen in the left side of the profile in Fig. 6(a) of [31]. Moreover, the overall direction of the systematic changes in the distribution is toward the Hillert 3D distribution.

The change of the GSDs throughout the entire simulation time implies that the GSDs shown in [31] do not correspond to that in the steady state. For computational efficiency, Krill and Chen turned on their coalescence-free algorithm only after a certain stage of the computation. However, the significant coalescence between grains occurred at the early stage, and as a result, its effect could be left even in the later stages of their simulation by slowing down the convergence rate to the steady state. The relatively high frequency of the larger grains in the Krill and Chen simulation as shown in Fig. 15 may be evidence for such effect of the coalescence. A similar feature can be found from the grain distribution with the number of faces per grain in Fig. 16, where the results from the vertex simulation [17] (triangles), Surface Evolver program [20] (circles), Krill and Chen [31] (squares), and the present study (stars) are compared. Again the higher frequency of the grains with more faces than 28 can be observed in the Krill and Chen data, while the frequency of such grains is negligible in the other three simulations where the coalescence between grains was prohibited throughout the entire computation time.

C. 3D von Neumann's law

The growth rate of each grain in the 2D system is strictly governed by the von Neumann-Mullins law (2); it depends on grain topology only, irrespective of the precise geometry. Mullins [57] has found a corresponding 3D growth law under the assumption that grains are regular polyhedra. Glazier [58] also has observed that there is a correlation between the growth rate and the number of faces of a grain in the 3D Potts model simulations. Following these findings, more elaborate statistical versions [59,60] of this 3D von Neumann have been proposed and compared with the simulation results [20,59,61] of the Surface Evolver program. In this section we compare the growth rates from the present simulation with the proposed versions of the 3D law.

The general form of the 3D von Neumann law takes the form

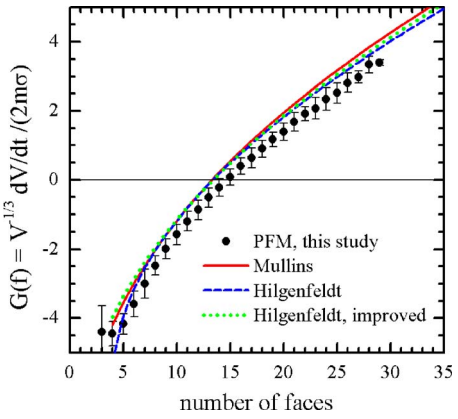

FIG. 17. (Color online) Change of $V^{-1/3}dV/dt/(2m\sigma)$ as a function of the number of faces per grain. The solid, dashed, and dotted curves denote the Mullins equation [57], Hilgenfeldt's equation [59], and its improved form [60], respectively. Filled circles are the present simulation results, which were obtained from the volume change rates of 2837 grains at $t=3000\Delta t$ during a single computation time step.

$$V^{-1/3}\frac{dV}{dt} = 2m\sigma G(f), \tag{21}$$

where V is the grain volume and f is the number of faces per grain. In the Mullins' approach [57], the function $G(f)$ is given by

$$G(f) = \frac{1}{2}\left(\frac{3}{4\pi}\right)^{1/3} G_1(f)G_2(f), \tag{22}$$

where

$$G_1(f) = \frac{\pi}{3} - 2\tan^{-1}\left(\frac{1.86(f-1)^{1/2}}{f-2}\right), \tag{23}$$

$$G_2(f) = 5.35f^{2/3}\left(\frac{f-2}{2(f-2)^{1/2}} - \frac{3}{8}G_1(f)\right)^{-1/3}. \tag{24}$$

For 3D bubble growth, Hilgenfeldt *et al.* [59] derived a different form:

$$G(f) = \frac{3}{2^{1/3}}\left(\frac{\pi}{3} - \chi_f\right)\left((f-2)\tan\left(\frac{\pi}{n_f}\right)\right)^{2/3}\tan^{1/3}\left(\frac{\chi}{2}\right), \tag{25}$$

where $n_f=6-12/f$ and

$$\chi_f = 2\tan^{-1}\sqrt{4\sin^2(\pi/n_f) - 1}. \tag{26}$$

Also Hilgenfeldt *et al.* [60] improved their growth law by using Mullins' method without the pentagonal-face approximation.

Figure 17 shows the change of $V^{-1/3}dV/dt/(2m\sigma)$ as a function of the number of faces per grain, where the solid, dashed, and dotted curves denote the Mullins equation, Hilgenfeldt's equation, and its improved form [60], respectively. Filled circles represent the results from the present simulation, which were obtained from the volume change rates of 2837 grains at $t=3000\Delta t$ during a single computation time step. Several points can be noticed from this figure. First, the simulation results appear to be almost parallel to the predictions, with a shift of about $\delta f \simeq 1$. The neutral number of faces satisfying $G(f_0)=0$ is $f_0=14.7$ in simulations, whereas $f_0=13.5$ in predictions. Second, the original equation (22) by Hilgenfeldt *et al.* seems to fit best with the simulation data, even though all three predictions are very close to each other. Third, the discrepancy between the simulations and predictions becomes larger with increasing number of faces. All these features have already been observed in the Surface Evolver simulations [20,59,61]. Thus the present large-scale simulation by phase-field model confirms the 3D growth law obtained from the Surface Evolver simulations in much smaller scales.

VI. CONCLUSION

The main problem in large-scale phase-field simulations of grain growth has been the limits in memory and computational time. We developed a simple, but powerful, computation scheme based on observation that the multiple junctions where more than six grains meet together at a point are extremely rare. In the phase-field simulation with this new computation scheme, an unlimited number of orientation variables can be allowed with high computation efficiency, independent of the number of the orientation variables. Large-scale phase-field simulations of the ideal grain growth on a 2400×2400 grid system in 2D and a $420\times420\times420$ in 3D could be carried out with holding the coalescence-free condition, where a few tens of thousands grains evolved into a few thousand grains.

By testing how well individual grains in the 2D simulations satisfy the von Neumann-Mullins law, it could be shown that our simulations were correctly operating under the conditions of ideal grain growth. The steady-state GSD in 2D appeared as a symmetrical shape with a plateau slightly inclined to the large grain side, which was quite different from the Hillert 2D distribution. The existence of the plateau stems from the wide separation of the peaks in the GSDs of the grains with five, six, and seven faces. For deeper understanding of the 2D ideal grain growth, including the existence of the plateau in the GSD, analysis of size distributions for each class may be needed.

The steady-state GSD in the 3D simulation of the ideal grain growth appeared to be very close to the Hillert 3D distribution in every respect; the asymmetry in the profile, a peak at $r=(9/8)\langle r\rangle$ and cut-off around. Such congruence was independent of the initial conditions such as GSD and average grain size. The mean-field assumption in 3D appeared to be a quite good representation for the growth rate of each grain. Also the Lifshitz-Slyozov stability condition which leads the system to the existence of a steady state was well satisfied in 3D simulation. Thus the Hillert theory can be regarded as an accurate description for the 3D ideal grain growth.

The dependence of the growth rate in 3D simulations on the grain topology was discussed. The large-scale phase-field simulation confirms the 3D growth law obtained from the Surface Evolver simulations in smaller scales.

ACKNOWLEDGMENTS

S.G.K. and W.T.K. are thankful for the financial support from Korea Science and Engineering Foundation through a basic research grant program [R01-200 2-000-00181-0(2002)]. Y.B.P. is indebted to Ministry of Commerce, Industry and Energy through the Regional Research Center of Sunchon National University for financial support.

[1] F. J. Humphreys and M. Hatherly, *Recrystallization and Related Annealing Phenomena* (Pergamon, Oxford, 1995).
[2] D. Raabe, *Computational Materials Science* (Wiley-VCH, Weinheim, Germany, 1998).
[3] M. P. Anderson, D. J. Srolovitz, G. S. Grest, and P. S. Sahn, Acta Metall. **32**, 783 (1984).
[4] D. J. Srolovitz, M. P. Anderson, P. S. Sahni, and G. S. Grest, Acta Metall. **32**, 793 (1984).
[5] S. Xiaoyan, L. Guoquan, and G. Nanju, Scr. Mater. **43**, 355 (2000).
[6] M. W. Nordbakke, N. Ryum, and O. Hunderi, Acta Mater. **50**, 3661 (2002).
[7] C. Wang and G. Liu, Mater. Lett. **57**, 4424 (2003).
[8] Y. Saito, Mater. Sci. Eng., A **223**, 114 (1997).
[9] Y. Saito, ISIJ Int. **38**, 559 (1998).
[10] O. M. Ivasishin, S. V. Shevchenko, N. L. Vasiliev, and S. L. Semiatin, Acta Mater. **51**, 1019 (2003).
[11] S. P. A. Gill and A. C. F. Cocks, Acta Mater. **44**, 4777 (1996).
[12] F. Cleri, Physica A **282**, 339 (2000).
[13] D. Moldovan, D. Wolf, S. R. Phillpot, and A. J. Haslam, Acta Mater. **50**, 3397 (2002).
[14] D. Moldovan, D. Wolf, S. R. Phillpot, and A. J. Haslam, Philos. Mag. A **82**, 1271 (2002).
[15] C. Maurice, in Proceedings of the 1st Joint International Conference on Recrystallization and Grain Growth, edited by G. Gottstein and D. A. Molodov (Springer, Aachen, Germany, 2001), p. 123.
[16] K. Fuchizaki and K. Kawasaki, Physica A **221**, 202 (1995).
[17] D. Weygand and Y. Brechet, Philos. Mag. B **79**, 703 (1999).
[18] K. Marthinsen, O. Hunderi, and N. Ryum, Acta Mater. **44**, 1681 (1996).
[19] C. Monnereau, N. Pittet, and D. Weaire, Europhys. Lett. **52**, 361 (2000).
[20] F. Wakai F, N. Eonomoto, and H. Ogawa, Acta Mater. **48**, 1297 (2000).
[21] H. J. Frost, C. V. Thompson, C. L. Howe, and J. Whang, Scr. Metall. **22**, 65 (1988).
[22] W. Fayad, C. V. Thompson, and H. J. Frost, Scr. Mater. **40**, 1199 (1999).
[23] Y. Liu, T. Baudin, and R. Penelle, Scr. Mater. **34**, 1679 (1996).
[24] J. Geiger, A. Roosz, and P. Barkoczy, Acta Mater. **49**, 623 (2001).
[25] A. Kuprat, D. George, G. Straub, and M. C. Demirel, Comput. Mater. Sci. **28**, 199 (2003).
[26] D. Fan and L. Q. Chen, Acta Mater. **45**, 611 (1997).
[27] D. Fan, C. Geng, and L. Q. Chen, Acta Mater. **45**, 1115 (1997).
[28] A. Kazaryan, Y. Wang, S. A. Dregia, and B. R. Patton, Phys. Rev. B **63**, 184102 (2001).
[29] A. Kazaryan, B. R. Patton, S. A. Dregia, and Y. Wang, Acta Mater. **50**, 499 (2002).
[30] A. Kazaryan, Y. Wang, S. A. Dregia, and B. R. Patton, Acta Mater. **50**, 2491 (2002).
[31] C. E. Krill III and L. Q. Chen, Acta Mater. **50**, 3059 (2002).
[32] M. Hillert, Acta Metall. **13**, 227 (1965).
[33] R. Kobayashi, Physica D **63**, 410 (1993).
[34] J. A. Warren and W. J. Boettinger, Acta Metall. Mater. **43**, 689 (1995).
[35] I. Tiaden, B. Nestler, H. J. Dipers, and I. Steinbach, Physica D **115**, 73 (1998).
[36] A. Karma and W. J. Rappel, Phys. Rev. E **57**, 4323 (1998).
[37] S. G. Kim, W. T. Kim, and T. Suzuki, Phys. Rev. E **60**, 7186 (1999).
[38] I. Steinbach and F. Pezzolla, Physica D **134**, 385 (1999).
[39] S. G. Kim, W. T. Kim, T. Suzuki, and M. Ode, J. Cryst. Growth **261**, 135 (2004).
[40] S. M. Allen and J. Cahn, Acta Metall. **27**, 1085 (1979).
[41] J. von Neumann, *Metal Interface* (ASM, Cleveland, Ohio, 1952), p. 108.
[42] W. W. Mullins, J. Appl. Phys. **27**, 900 (1956).
[43] G. Abbruzzese, I. Heckelmann, and K. Lücke, Acta Metall. Mater. **40**, 519 (1992).
[44] K. Lücke, I. Heckelmann, and G. Abbruzzese, Acta Metall. Mater. **40**, 533 (1992).
[45] W. W. Mullins, Acta Mater. **46**, 6219 (1998).
[46] C. Lou and M. A. Player, J. Phys. D **34**, 1286 (2001).
[47] P. R. Rios and K. Lücke, Scr. Mater. **44**, 2471 (2001).
[48] C. S. Pande and A. K. Rajagopal, Acta Mater. **49**, 1805 (2001).
[49] P. E. Di Nunzio, Acta Mater. **49**, 3635 (2001).
[50] T. O. Saetre, Acta Mater. **50**, 1539 (2002).
[51] C. S. Pande and A. K. Rajagopal, Acta Mater. **50**, 3013 (2002).
[52] L. Helfen, D. T. Wu, R. Birringer, and C. E. Krill III, Acta Mater. **51**, 2743 (2003).
[53] M. W. Norbakke, N. Ryum, and O. Hunderi, Mater. Sci. Forum **467-470**, 1081 (2004)
[54] P. R. Rios, Acta Mater. **52**, 249 (2004).
[55] P. R. Rios and K. Lücke, Scr. Mater. **44**, 2471 (2001).
[56] M. Lifshitz and V. V. Slyozov, J. Phys. Chem. Solids **19**, 35 (1961).
[57] W. W. Mullins, Acta Metall. **37**, 2979 (1989).
[58] J. A. Glazier, Phys. Rev. Lett. **70**, 2170 (1993).
[59] S. Hilgenfeldt, A. M. Kraynik, S. A. Koehler, and H. A. Stone, Phys. Rev. Lett. **86**, 2685 (2001).
[60] S. Hilgenfeldt, A. M. Kraynik, D. Reinelt, and J. Sullivan, Europhys. Lett. **67**, 484 (2004).
[61] S. Jurine, S. Cox, and F. Graner, Colloids Surf., A **263**, 16 (2005).